LETTER

https://doi.org/10.1038/s41586-018-0486-3

Superluminal motion of a relativistic jet in the neutron-star merger GW170817

K. P. Mooley[1,2,10]*, A. T. Deller[3,4,10], O. Gottlieb[5,10]*, E. Nakar[5], G. Hallinan[2], S. Bourke[6], D. A. Frail[1], A. Horesh[7], A. Corsi[8] & K. Hotokezaka[9]

The binary neutron-star merger GW170817[1] was accompanied by radiation across the electromagnetic spectrum[2] and localized[2] to the galaxy NGC 4993 at a distance[3] of about 41 megaparsecs from Earth. The radio and X-ray afterglows of GW170817 exhibited delayed onset[4–7], a gradual increase[8] in the emission with time (proportional to $t^{0.8}$) to a peak about 150 days after the merger event[9], followed by a relatively rapid decline[9,10]. So far, various models have been proposed to explain the afterglow emission, including a choked-jet cocoon[4,8,11–13] and a successful-jet cocoon[4,8,11–18] (also called a structured jet). However, the observational data have remained inconclusive[10,15,19,20] as to whether GW170817 launched a successful relativistic jet. Here we report radio observations using very long-baseline interferometry. We find that the compact radio source associated with GW170817 exhibits superluminal apparent motion between 75 days and 230 days after the merger event. This measurement breaks the degeneracy between the choked- and successful-jet cocoon models and indicates that, although the early-time radio emission was powered by a wide-angle outflow[8] (a cocoon), the late-time emission was most probably dominated by an energetic and narrowly collimated jet (with an opening angle of less than five degrees) and observed from a viewing angle of about 20 degrees. The imaging of a collimated relativistic outflow emerging from GW170817 adds substantial weight to the evidence linking binary neutron-star mergers and short γ-ray bursts.

Our very long-baseline interferometry (VLBI) observations with the High Sensitivity Array (HSA)—which consists of the Very Long Baseline Array (VLBA), the Karl G. Jansky Very Large Array (VLA) and the Robert C. Byrd Green Bank Telescope (GBT)—75 and 230 days after the GW170817 merger event (mean epochs; see Methods) indicate that the centroid position of the radio counterpart of GW170817 changed from a right ascension of RA = 13 h 09 min 48.068638(8) s and declination of dec. = −23° 22′ 53.3909(4)″ to RA = 13 h 09 m in 48.068831(11) s and dec. = −23° 22′ 53.3907(4)″ between these epochs (1σ uncertainties in the last digits are given in parentheses). This implies an positional offset between the two observations of $2.67 \pm 0.19 \pm 0.21$ mas in RA and $0.2 \pm 0.6 \pm 0.7$ mas in dec. (1σ uncertainties; statistical and systematic, respectively; see Methods). This corresponds to a mean apparent velocity of the source of the radio counterpart along the plane of the sky of $\beta_{\rm app} = 4.1 \pm 0.5$, where $\beta_{\rm app}$ is in units of the speed of light, c (1σ, including the uncertainty in the source distance). Offset positions of the radio source and the positional uncertainties at both VLBI epochs are shown in Fig. 1. Our VLBI data are consistent with the source being unresolved at both day 75 and day 230. Given the VLBI angular resolution and the signal-to-noise ratio of the detection, this puts an upper limit on the size of the source in both epochs of about 1 mas (0.2 pc at the distance of NGC 4993) in the direction parallel to its motion and 10 mas perpendicular to its motion (see Methods).

The substantial proper motion of the radio source immediately rules out isotropic ejecta models[21–23] for the radio (and X-ray) afterglow, which predict proper motion close to zero, and argues in favour of highly anisotropic ejecta (consistent with jet models). If the ejecta are bipolar, then one of the components is relativistically beamed into our line of sight.

Although superluminal motion is seen frequently in active galactic nuclei and micro-quasars, it is extremely rare in extragalactic explosive transients. Superluminal motion has been measured in only one such transient: the long-duration γ-ray burst GRB 030329[24]. GRB 030329 had a measured superluminal expansion of $\beta_{\rm app} \approx 3$–5, but no proper motion, whereas GW170817 has measured proper motion, but no expansion. Although both were relativistic events of comparable energies, these differences suggest different geometries and/or viewing angles.

The apparent velocity and size of a source moving at relativistic speeds, such as the radio counterpart of GW170817, differs from its actual velocity and size. The image of a point source, moving at a Lorentz factor Γ and viewed at an angle θ, is point-like and has a maximal apparent velocity of $\beta_{\rm app} = \Gamma$, which is obtained when $\theta = 1/\Gamma$. On the other hand, the maximal centroid velocity of an extended source with a uniform Γ is less than Γ, and its image size increases[25] with the source size and with Γ. An extreme example of the latter case is a spherically symmetric source expanding isotropically. In such a case, the image is a ring with a radius that increases at a velocity Γ with no centroid motion. The centroid velocity may also be affected in cases where we see different regions of the outflow at different times[26] (that is, a pattern motion).

Using this information, we examine the results from the VLBI data and the radio light curve to derive analytical constraints on the geometry and size of the radio source. We assume that the ejecta are axis-symmetric, so that $\theta_{\rm obs}$ is the viewing angle and $\theta_{\rm s}$ is the average angular size of the source that dominates the emission between 75 and 230 days after the merger (both with respect to the symmetry axis). If the source is compact ($\theta_{\rm s} \lesssim \theta_{\rm obs} - \theta_{\rm s}$), its size and possible pattern motion have only a small effect on the observed radiation and so we can use the point-source approximation. In all of the highly aspherical models suggested, the energy density increases towards the axis of symmetry, implying that during the peak of the light curve the emission is dominated by a region at $(\theta_{\rm obs} - \theta_{\rm s}) \approx 1/\Gamma$. Using the point-source approximation, this implies that between the two observations the source is observed at an angle of $(\theta_{\rm obs} - \theta_{\rm s}) \approx 1/\beta_{\rm app} \approx 0.25$ rad and its Lorentz factor is $\Gamma \approx \beta_{\rm app} \approx 4$. If the source is extended ($\theta_{\rm s} \gg \theta_{\rm obs} - \theta_{\rm s}$), then to achieve the observed apparent velocity the source should have $\Gamma > 4$ and possibly $\theta_{\rm obs} - \theta_{\rm s} < 0.25$ rad.

There are several strong lines of evidence that suggest that the source is compact. First, it is very compact in our VLBI observations, and is consistent with being unresolved. Second, the observed flux depends

[1]National Radio Astronomy Observatory, Socorro, NM, USA. [2]Caltech, Pasadena, CA, USA. [3]Centre for Astrophysics and Supercomputing, Swinburne University of Technology, Hawthorn, Victoria, Australia. [4]ARC Centre of Excellence for Gravitational Wave Discovery (OzGrav), Hawthorn, Victoria, Australia. [5]The Raymond and Beverly Sackler School of Physics and Astronomy, Tel Aviv University, Tel Aviv, Israel. [6]Department of Space, Earth and Environment, Chalmers University of Technology, Onsala Space Observatory, Onsala, Sweden. [7]Racah Institute of Physics, The Hebrew University of Jerusalem, Jerusalem, Israel. [8]Department of Physics and Astronomy, Texas Tech University, Lubbock, TX, USA. [9]Department Astrophysical Sciences, Princeton University, Princeton, NJ, USA. [10]These authors contributed equally: K. P. Mooley, A. T. Deller, O. Gottlieb. *e-mail: kunal@astro.caltech.edu; oregottlieb@gmail.com

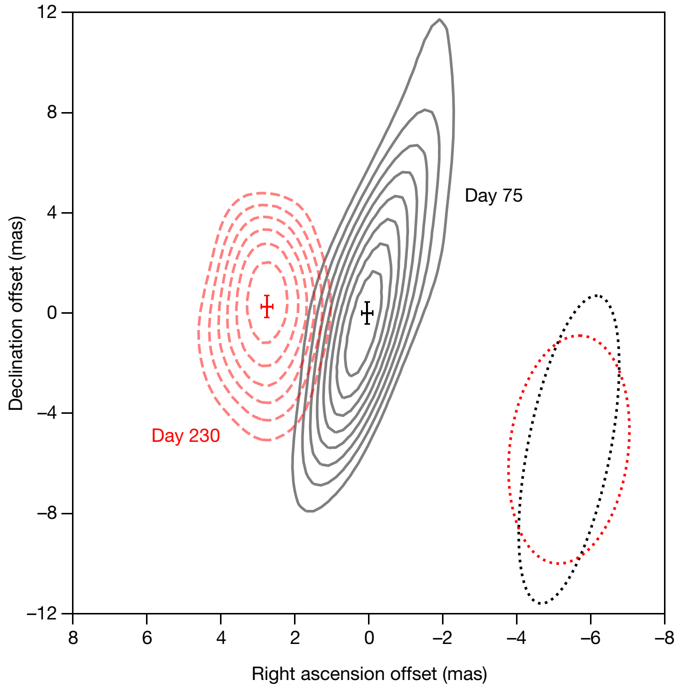

Fig. 1 | Proper motion of the radio counterpart of GW170817. The offset positions of the centroid (shown by 1σ error bars) and 3σ–12σ contours of the radio source detected 75 days (black) and 230 days (red) after the merger event using VLBI at 4.5 GHz. The two VLBI epochs have image root-mean-square noise of 5.0 μJy beam^{-1} and 5.6 μJy beam^{-1} (natural weighting), respectively, and the peak flux densities of GW170817 are 58 μJy beam^{-1} and 48 μJy beam^{-1}, respectively. The radio source is consistent with being unresolved at both epochs. The shapes of the synthesized beams for the images from each epoch are shown as dotted ellipses in the lower right corner. The proper-motion vector of the radio source has a magnitude of 2.7 ± 0.3 mas and a position angle of 86° ± 18°, measured over 155 days.

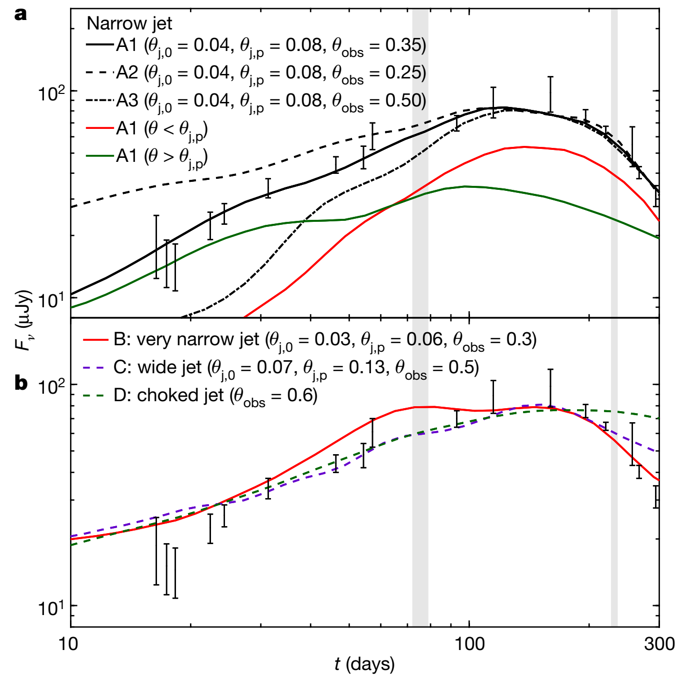

Fig. 2 | Radio, 3-GHz light curves of several representative simulated models. The black error bars (1σ) are the 3-GHz flux density (F_ν) values for GW170817. The grey shaded regions denote the VLBI epochs: 75 and 230 days after the merger. **a**, A narrow jet with an initial opening angle of $\theta_{j,0} = 0.04$ rad (2.3°), total energy of $E = 10^{50}$ erg and isotropic equivalent energy of $E_{iso} = 10^{53}$ erg at the core, as observed at three different viewing angles (models A1–A3). For all light curves, we take the energy fraction of accelerated electrons to be $\varepsilon_e = 0.1$, assume a power-law index of $p = 2.16$, and vary the energy fraction of the magnetic field ε_B and the external density n (which is assumed to be constant in space) to obtain a best fit to the light curve. The opening angle of the jet core at the time of the peak is $\theta_{j,p} = 0.08$ rad. The model that gives best fits both for the light curve and the images corresponds to a viewing angle of $\theta_{obs} = 0.35$ rad ($\varepsilon_B = 10^{-4}$, $n = 6 \times 10^{-4}$ cm^{-3}). The red line shows the contribution of emission from the jet core ($\theta < \theta_{j,p}$) and the green line shows the cocoon emission. The fit to the observations is obtained only in a narrow range of viewing angles. For smaller angles (such as $\theta_{obs} = 0.25$ rad, $\varepsilon_B = 2 \times 10^{-4}$, $n = 10^{-4}$ cm^{-3}) the light curve rises too slowly and the image centroid moves too far, whereas at larger angles (such as $\theta_{obs} = 0.5$ rad, $\varepsilon_B = 8 \times 10^{-5}$, $n = 6 \times 10^{-3}$ cm^{-3}) the light curve rises too quickly and the image centroid motion is too small. **b**, Light curves of three other models. Model B: another narrow jet with a lower energy, $\theta_{j,p} = 0.06$ rad, $E = 10^{49}$ erg and $E_{iso} = 2 \times 10^{52}$ erg ($\varepsilon_B = 4 \times 10^{-5}$, $n = 7 \times 10^{-3}$ cm^{-3}), at $\theta_{obs} = 0.3$ rad, which provides a reasonable fit to the data. Model C: a wider jet with $\theta_{j,p} = 0.13$ rad; even for $\theta_{obs} = 0.5$ rad, the light curve does not decay fast enough to be consistent with the most recent data points, and at this viewing angle the image centroid moves too slowly. Model D: a model of a choked jet; the light curve does not decay fast enough after the peak and the image motion, although superluminal, is very slow compared to the observations. In all of the models that we considered, the spectrum between radio and X-ray frequencies follows a constant power law (cooling and self-absorption do not affect this spectral range) and so models that fit the radio, 3-GHz data fit the entire afterglow observations from radio to X-ray frequencies; see Methods for details.

very strongly on Γ (as roughly $\Gamma^{10.4}$), which implies that on day 150 the Lorentz factor of the radio source was[19] less than about 5. Last, and most constraining, is the rapid turnover around the peak of the radio light curve and the very fast decline that follows $F_\nu \propto t^{-2}$ after day 200, where F_ν is the flux density and t is the time in the observer frame (K.P.M. et al., manuscript in preparation). The shape of the peak and the following decline depends on the ratio $\theta_s/(\theta_{obs} - \theta_s)$. A smaller ratio results in a narrower peak, and if $\theta_s \gg \theta_{obs} - \theta_s$ the decay is expected to be[19] at first roughly linear in time, whereas if $\theta_s \ll \theta_{obs} - \theta_s$ the flux decay after the peak is predicted to behave as roughly $F_\nu \propto t^{-p}$, where the radio spectrum dictates[8,12,16] that $p \approx 2.16$. We conclude that the combination of the image and the light curve indicate that around the peak, at day 150, the emission is most probably dominated by a narrow component with $\theta_s \ll 0.25$ rad and $\Gamma \approx 4$, which is observed at an angle of $\theta_{obs} - \theta_s \approx 0.25$ rad (in contrast to the emission during the first month or two, which was most probably dominated by cocoon emission from angles larger than θ_s).

The constraints derived above strongly disfavour an uncollimated choked jet, where the jet has a wide opening angle and does not successfully escape the neutron-rich material ejected dynamically during the merger (that is, it is choked and so does not contain a relativistic narrow core). A narrowly collimated choked jet may generate an outflow with a narrow high-energy core, but it is hard to obtain a Lorentz factor that is high enough without a fine tuning of the location where the jet is choked. In contrast to all other models, the successful-jet model predicts a structure that can easily satisfy the constraints of the image and the light curve. In this model, the gradual rise is generated by cocoon emission and the peak is observed when the core of the successful jet decelerates and starts to dominate the emission. The jet opening angle θ_j and its Lorentz factor are those of the source in our images around the time of the peak, namely $\theta_j \approx \theta_s$. We can only put a lower limit on the initial Lorentz factor of the jet Γ_0, because we do not know the deceleration radius (that is, when the transition from the coasting phase to the power-law decline phase took place). All of the observational data can be explained with a narrowly collimated jet with $\Gamma_0 \gtrsim 10$.

To verify the analytical considerations discussed above, and to find tighter constraints on the outflow, we ran a set of relativistic hydrodynamic simulations (see Methods). Our simulations include configurations of choked and successful jets at various opening angles and

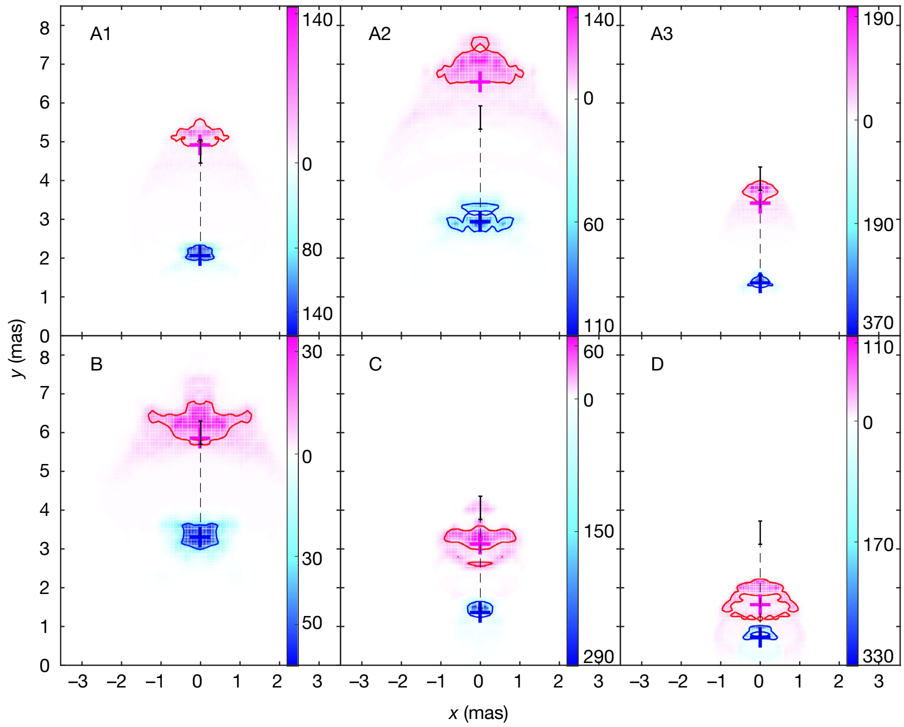

Fig. 3 | Synthetic radio images. Each panel shows two colour maps of the flux density (in units of μJy mas^{-2}), one at day 75 (blue colour palette) and one at day 230 (magenta colour palette), for the models A1–A3, B, C and D shown in Fig. 2. The position at the time of the merger is $x = y = 0$, and the blue and magenta crosses mark the flux centroid at days 75 and 230, respectively. The 50% flux containment contours are also shown at the two epochs. The black dashed lines mark the direction of centroid motion and the black solid segments denote the motion consistent with the VLBI observations within 1σ, 2.7 ± 0.3 mas. Only models A1 and B, which are of narrow jets ($\theta_{j,p} < 0.1$ rad) observed at angles of $\theta_{obs} = 0.35$ rad and $\theta_{obs} = 0.3$ rad, respectively, show centroid motions that are consistent with the observations (2.8 mas and 2.6 mas, respectively). These are also the models that provide the best fits to the light curve. The centroid motion between the two epochs of successful-jet models with larger opening angle ($\theta_{obs} = 0.5$ rad), A3 and C, is too small (2.1 mas and 1.7 mas, respectively); that of model A2 ($\theta_{obs} = 0.25$ rad) is too large (3.5 mas). The centroid motion for the choked-jet model, D, is much too small (0.7 mas). In all of the successful-jet models, larger viewing angles lead to more compact images. The observed images were unresolved, with an upper limit on the width parallel to the centroid motion of about 1 mas (1σ). Models A1, A3 and C ($\theta_{obs} \geq 0.35$ rad) are consistent with this limit, model B ($\theta_{obs} = 0.3$ rad) is marginal and model A2 ($\theta_{obs} = 0.25$ rad) is too extended. See Fig. 2 and Methods for further details of the various models and their fitting to the VLBI data.

viewing angles, and include emission from all components of the outflow. In Fig. 2 we show light curves from six different configurations, and in Fig. 3 the corresponding images at days 75 and 230. As expected, we find that in simulations in which the jet is choked, the centroid velocity of the images is too slow to explain the proper motion of GW170817, and the decline of the light curve after the peak is much slower than t^{-2}. Among the successful-jet simulations, those that correspond to jets observed from a large angle ($\theta_{obs} - \theta_j \gtrsim 0.4$ rad) did not produce images that moved fast enough; on the other hand, in the simulation of jets that were observed at an angle that is too small ($\theta_{obs} - \theta_j \lesssim 0.2$ rad), the image centroid moved too fast and/or the source size was too large. The light curve also constrains the geometry, and only simulations with $\theta_j/(\theta_{obs} - \theta_j)$ small enough can fit the rapid transition from a rising light curve to the observed decay. Of all of the configurations that we examined, only extremely narrow jets with $\theta_j < 0.1$ rad that were observed at an angle of $0.2\ \text{rad} < \theta_{obs} - \theta_j < 0.4$ rad result in emission that is consistent with the light curve and that reproduces the observed motion of the image centroid. Taken together, these results imply that we see a narrow jet with $\theta_j < 0.1$ rad ($<5°$) from a viewing angle in the range $0.25\ \text{rad} < \theta_{obs} < 0.50$ rad (14°–28°). This can be seen, for example, in Figs. 2 and 3, in which the centroid motion for models with viewing angles outside of this range deviate significantly (by more than 2σ; see Methods) from the observations, and models with wider jets ($\theta_j > 0.1$ rad) do not reproduce the rapid decay after the peak in the light curve. In a different study[27], we carried out a full scan of the parameter space using two different semi-analytical jet structures, and the values obtained for θ_j and θ_{obs} lie within the ranges specified above.

Our simulation that provides the best fit to the data is of a 0.08-rad (4° at the time of light-curve peak) jet that is observed from $\theta_{obs} = 0.35$ rad (20°). In this simulation, the cocoon dominates the observed radio emission until about day 60, after which time the jet dominates (see Fig. 2 and Methods). The Lorentz factor of the observed region decreases slowly from $\Gamma \approx 4$ on day 75 to $\Gamma \approx 3$ on day 230. Within the framework of standard afterglow theory from a successful jet, the observations put tight constraints on additional properties of the jet and the surrounding environment (see Methods). The total energy of the relativistic ejecta (jet + cocoon) is in the range 10^{49}–10^{50} erg and the external density is 10^{-4} cm^{-3} to 5×10^{-3} cm^{-3}. Figure 4 illustrates the physical and geometric parameters that we derive for GW170817.

Our final model is qualitatively similar to jet + cocoon (also referred to as structured jet) models suggested previously[13,15,16,28]. However, owing to the VLBI data and more up-to-date light curves, our constraints on the opening and viewing angles of the jet are much tighter than those obtained from previous models, and in tension with some. The small viewing angle (around 20°) for GW170817 is expected in only about 5% of the mergers (not accounting for the gravitational-wave polarization bias). Our best-fitting model suggests we were relatively lucky with GW170817 because the afterglow of this event as observed at larger angles would be much fainter. In our best-fitting numerical model, the radio emission should be detectable at a viewing angle of about 30°, but would probably be too faint for detection at an angle of about 40°. The detectability of future GW170817-like events depends on the circum-merger density. Taking our best-fitting model for GW170817, but increasing the density to 0.01 cm^{-3} (the median

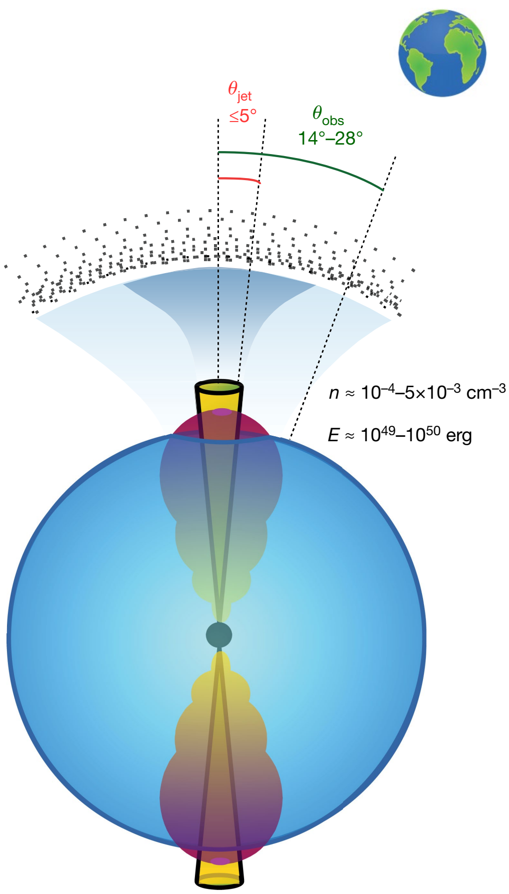

Fig. 4 | Schematic of the physical and geometric parameters derived for GW170817. GW170817 has a successful jet (yellow) that drives a cocoon (red) through interaction with the dynamical ejecta (blue). This scenario is the same as scenario E in our previous work[8] and consistent with structured-jet models. The shock breakout from the cocoon probably produced the γ-ray signal and the cocoon's interaction with the interstellar medium produced the early-time (up to about two months after the merger) radio and X-ray emission. The relativistic core of the jet has a half-opening angle of $\theta_{jet} \leq 5°$. Earth is located $\theta_{obs} = 14°$–$28°$ away from the core of the jet. GW170817 most probably gave rise to a SGRB pointing at such an angle away from Earth. The interaction between the jet and the interstellar medium produced the late-time radio and X-ray emission. Our VLBI measurement suggests that the Lorentz factor of the jet 150 days after the merger (at the peak of the radio light curve, when the core of the jet came into view) is $\Gamma \approx 4$. The total energy (E) of the jet and cocoon system is 10^{49}–10^{50} erg. The density (n) of the circum-merger environment is 10^{-4}–5×10^{-3} cm^{-3}.

density[29] for short GRBs (SGRBs); while keeping all other values constant), we find an afterglow that is brighter by about an order of magnitude at the peak compared to that of GW170817. Such an afterglow could have been detected at a distance of 40 Mpc at a larger viewing angle of about 50°.

Our VLBI result implies that binary neutron-star mergers launch relativistic, narrowly collimated jets that successfully penetrate the dynamical ejecta, which is a prerequisite for the production of SGRBs (which require $\Gamma_0 \gtrsim 100$). If GW170817 produced an SGRB pointing away from us, then its peak isotropic equivalent luminosity in γ-rays was $L_{iso} \approx 10^{52}$ erg s^{-1} when observed within the jet cone, assuming that the initial opening angle of the jet was around 0.05 rad. The rate of SGRBs with a peak L_{iso} of more than about 10^{52} erg s^{-1} is only[30] about 0.1 Gpc^{-3} yr^{-1}, corresponding to about 1% of all SGRBs that point towards Earth. This suggests either that we were extremely lucky to observe such an event or that all such luminous events are more narrowly beamed than events of smaller L_{iso} and do not typically point towards Earth. For example, if GW170817, with an opening angle of approximately 0.05 rad, is representative of events with $L_{iso} \approx 10^{52}$ erg s^{-1}, it would imply that there are 1,000 events with such luminosity that point away from Earth for every SGRB-producing event that points towards Earth—that is, a rate of about 100 Gpc^{-3} yr^{-1} for GW170817-like events. This rate is about 3%–30% of the binary neutron-star merger rate[1] ($1{,}540^{+3{,}200}_{-1{,}220}$ Gpc^{-3} yr^{-1}) and would imply that the true fraction of high-luminosity SGRBs is much higher than observed at Earth. An anticorrelation between the opening angle of the jet and its isotropic equivalent energy is one possible cause for such a relationship, and follows naturally if the total energy of different events varies less than their beaming. This possibility can be easily tested with a small number of future events with off-axis afterglow emission.

Online content

Any methods, additional references, Nature Research reporting summaries, source data, statements of data availability and associated accession codes are available at https://doi.org/10.1038/s41586-018-0486-3.

Received: 19 June; Accepted: 7 August 2018;
Published online 5 September 2018.

1. Abbott, B. P. et al. GW170817: observation of gravitational waves from a binary neutron star inspiral. *Phys. Rev. Lett.* **119**, 161101 (2017).
2. Abbott, B. P. et al. Multi-messenger observations of a binary neutron star merger. *Astrophys. J.* **848**, L12 (2017).
3. Hjorth, J. et al. The distance to NGC 4993: the host galaxy of the gravitational-wave event GW170817. *Astrophys. J.* **848**, L31 (2017).
4. Hallinan, G. et al. A radio counterpart to a neutron star merger. *Science* **358**, 1579–1583 (2017).
5. Troja, E. et al. The X-ray counterpart to the gravitational-wave event GW170817. *Nature* **551**, 71–74 (2017).
6. Margutti, R. et al. The electromagnetic counterpart of the binary neutron star merger LIGO/Virgo GW170817. V. Rising X-ray emission from an off-axis jet. *Astrophys. J.* **848**, L20 (2017).
7. Haggard, D. et al. A deep Chandra X-ray study of neutron star coalescence GW170817. *Astrophys. J.* **848**, L25 (2017).
8. Mooley, K. P. et al. A mildly relativistic wide-angle outflow in the neutron-star merger event GW170817. *Nature* **554**, 207–210 (2018).
9. Dobie, D. et al. A turnover in the radio light curve of GW170817. *Astrophys. J.* **858**, L15 (2018).
10. Alexander, K. D. et al. A decline in the X-ray through radio emission from GW170817 continues to support an off-axis structured jet. *Astrophys. J.* **863**, L18 (2018).
11. Kasliwal, M. M. et al. Illuminating gravitational waves: A concordant picture of photons from a neutron star merger. *Science* **358**, 1559–1565 (2017).
12. Troja, E. et al. The outflow structure of GW170817 from late-time broad-band observations. *Mon. Not. R. Astron. Soc.* **478**, L18–L23 (2018).
13. Xie, X., Zrake, J. & MacFadyen, A. Numerical simulations of the jet dynamics and synchrotron radiation of binary neutron star merger event GW170817/GRB 170817A. *Astrophys. J.* **863**, 58 (2018).
14. Lamb, G. P. & Kobayashi, S. Electromagnetic counterparts to structured jets from gravitational wave detected mergers. *Mon. Not. R. Astron. Soc.* **472**, 4953–4964 (2017).
15. Lazzati, D. et al. Late time afterglow observations reveal a collimated relativistic jet in the ejecta of the binary neutron star merger GW170817. *Phys. Rev. Lett.* **120**, 241103 (2018).
16. Margutti, R. et al. The binary neutron star event LIGO/Virgo GW170817 160 days after merger: synchrotron emission across the electromagnetic spectrum. *Astrophys. J.* **856**, L18 (2018).
17. Lyman, J. D. et al. The optical afterglow of the short gamma-ray burst associated with GW170817. *Nat. Astron.* https://doi.org/10.1038/s41550-018-0511-3 (2018).
18. Resmi, L. et al. Low frequency view of GW 170817/GRB 170817A with the Giant Meterwave Radio Telescope. Preprint at https://arxiv.org/abs/1803.02768 (2018).
19. Nakar, E. & Piran, T. Implications of the radio and X-ray emission that followed GW170817. *Mon. Not. R. Astron. Soc.* **478**, 407–415 (2018).
20. Troja, E., Piro, L. & Ryan, G. Chandra observations of GW170817 reveal a fading afterglow. *Astron. Telegr.* 11619 (2018).
21. Hotokezaka, K., Kiuchi, K., Shibata, M., Nakar, E. & Piran, T. Synchrotron radiation from the fast tail of dynamical ejecta of neutron star mergers. Preprint at https://arxiv.org/abs/1803.00599 (2018).
22. D'Avanzo, P. et al. The evolution of the X-ray afterglow emission of GW 170817/GRB 170817A in XMM-Newton observations. *Astron. Astrophys.* **613**, L1 (2018).
23. Gill, R. & Granot, J. Afterglow imaging and polarization of misaligned structured GRB jets and cocoons: breaking the degeneracy in GRB 170817A. *Mon. Not. R. Astron. Soc.* **478**, 4128–4141 (2018).
24. Taylor, G., Frail, D., Berger, E. & Kulkarni, S. High resolution observations of GRB 030329. *AIP Conf. Ser.* **727**, 324–327 (2004).
25. Boutelier, T., Henri, G. & Petrucci, P.-O. The influence of the jet opening angle on the appearance of relativistic jets. *Mon. Not. R. Astron. Soc.* **418**, 1913–1922 (2011).

26. Lind, K. R. & Blandford, R. D. Semidynamical models of radio jets: relativistic beaming and source counts. *Astrophys. J.* **295**, 358–367 (1985).
27. Hotokezaka, K. et al. A Hubble constant measurement from superluminal motion of the jet in GW170817. Preprint at https://arxiv.org/abs/1806.10596 (2018).
28. Nakar, E., Gottlieb, O., Piran, T., Kasliwal, M. M. & Hallinan, G. From γ to radio - the electromagnetic counterpart of GW 170817. Preprint at https://arxiv.org/abs/1803.07595 (2018).
29. Fong, W., Berger, E., Margutti, R. & Zauderer, B. A. A decade of short-duration gamma-ray burst broadband afterglows: energetics, circumburst densities, and jet opening angles. *Astrophys. J.* **815**, 102 (2015).
30. Wanderman, D. & Piran, T. The rate, luminosity function and time delay of non-Collapsar short GRBs. *Mon. Not. R. Astron. Soc.* **448**, 3026–3037 (2015).

Acknowledgements We are grateful to the VLBA, VLA and GBT staff, especially M. Claussen, A. Mioduszewski, T. Minter, F. Ghigo, W. Brisken, K. O'Neill and M. McKinnon, for their support with the HSA observations. We thank V. Dhawan and P. Demorest for help with observational issues with the VLBI system at the VLA. K.P.M. thanks A. Mioduszewski, E. Momjian, E. Greisen, T. Pearson and S. Kulkarni for discussions. We thank M. Kasliwal for providing comments on the manuscript. The National Radio Astronomy Observatory is a facility of the National Science Foundation operated under cooperative agreement by Associated Universities. K.P.M. is currently a Jansky Fellow of the National Radio Astronomy Observatory. K.P.M. acknowledges support from the Oxford Centre for Astrophysical Surveys, which is funded through the Hintze Family Charitable Foundation, for some initial work presented here. E.N. acknowledges the support of an ERC starting grant (GRB/SN) and an ISF grant (1277/13). A.T.D. is the recipient of an Australian Research Council Future Fellowship (FT150100415). G.H. acknowledges the support of NSF award AST-1654815. A.H. acknowledges support by the I-Core Program of the Planning and Budgeting Committee and the Israel Science Foundation. A.C. acknowledges support from the NSF CAREER award number 1455090 titled 'CAREER: Radio and gravitational-wave emission from the largest explosions since the Big Bang'.

Author contributions K.P.M., A.T.D., S.B., G.H. and D.A.F. coordinated the VLBI observations. A.T.D. and K.P.M. performed the VLBI data processing. O.G. and E.N. carried out the theoretical study, including analytic calculations and numerical simulations, with some input from K.H. K.P.M., A.T.D., E.N., G.H. and D.A.F. wrote the paper. A.C. and A.H. compiled the references. A.H., A.D. and K.P.M. compiled Methods. O.G., A.T.D., A.H. and K.P.M. prepared the figures. All co-authors discussed the results and provided comments on the manuscript.

Competing interests The authors declare no competing interests.

Additional information

Extended data is available for this paper at https://doi.org/10.1038/s41586-018-0486-3.

Reprints and permissions information is available at http://www.nature.com/reprints.

Correspondence and requests for materials should be addressed to K.P.M. and O.G.

Publisher's note: Springer Nature remains neutral with regard to jurisdictional claims in published maps and institutional affiliations.

METHODS

Observations, data processing and basic analysis. To establish the size and morphology of the faint radio afterglow of GW170817, we obtained Director's Discretionary Time (programme ID BM469) to observe with the HSA. The HSA antennas included the ten VLBA dishes, the phased Karl G. Jansky VLA and the GBT, although not all stations were used in all observations. The maximum baseline was typically 7,500–8,000 km.

VLBI observations. We observed GW170817 with the HSA over four epochs between 2017 September and 2018 April. Each epoch consisted of 2–4 observations carried out over a period of up to 10 days, with approximately three hours of on-source time on GW170817 per day. The choice of the observing frequency was informed by the results from the VLA monitoring of the radio light curve, the desired angular resolution and the ease of scheduling on the telescopes. In all epochs, a total bandwidth of 256 MHz was sampled in dual polarization at 2-bit precision. Depending on the observing frequency, the recorded bandwidth was broken into eight 32-MHz-wide bands or two 128-MHz-wide bands. A summary of the observations is given in Extended Data Table 1.

The first epoch was undertaken in the L band (central frequency of 1,550 MHz) 37–38 days post-merger. No fringes were seen on the GBT on one of the two observing days owing to an unknown technical issue, considerably reducing overall sensitivity at this epoch. The second epoch was carried out in the S band (central frequency of 3,200 MHz), 51–52 days post-merger. However, a misconfiguration of the VLA correlator on both days meant that phased VLA data were practically unusable, and hence sensitivity was severely impacted. The third epoch was observed in the C band (central frequency of 4,540 MHz) 72–79 days post-merger. The fourth epoch was likewise observed in the C band, 227–236 days post-merger, using only the VLBA and VLA as the GBT was unavailable.

Each observation was structured around an 8-min cycle as follows. We used the source J1258−2219 (an approximately 1-Jy flat-spectrum source, separated by 2.8° from GW170817) as the primary delay and gain calibrator, visiting it twice per cycle during the first three epochs and once per cycle in the fourth epoch of observations. J1312−2350, a 20-mJy source separated by 0.8° from GW170817, was used as a secondary phase calibrator, and was visited once per cycle in the first three epochs and twice per cycle in the fourth epoch of observations. J1258−2219 was additionally used to determine phase solutions for the VLA once per cycle. A single scan on 3C286 was included at the end of each observation to allow flux calibration of the commensally recorded VLA interferometer data. For the C-band (4.5 GHz) epochs only, we included three scans on the blazar OQ208 (B1404+286) over the course of each observation to enable polarization calibration to be determined and applied.

VLBI data processing. We followed standard data-reduction procedures for HSA data using the AIPS software package[31]. For all calibration steps that involve a sky source (fringe-fitting, leakage and self-calibration) we used a model of the source that was iteratively refined over several passes of the entire data-reduction pipeline.

The data was loaded using 'FITLD' and a priori amplitude corrections were applied using 'ANTAB' and 'ACCOR'. An issue with the VLA automatic gain control was uncovered whereby the phased VLA data exhibited large short-term amplitude variations; this could be (and was) largely mitigated by using a per-integration solution for the auto-correlation-based corrections with 'ACCOR', but small residual variations that were weakly detrimental to sensitivity remained. This problem was fixed before the fourth observational epoch. 'CLCOR' was used to correct for parallactic angle rotation and to apply the most accurate available values for Earth orientation parameters. 'TECOR' was used to correct for ionospheric propagation effects, using the 'igsg' model available from ftp://cddis.gsfc.nasa.gov/gps/products/ionex. We then calibrated the time-independent delays and the antenna bandpass using 'FRING' and 'BPASS'; in the first two epochs we used a scan on the primary calibrator J1258–2219, whereas in the third and fourth epochs we used OQ208.

For the third epoch at 4.5 GHz only, we calibrated the cross-polar delays and instrumental polarization leakage using the tasks 'FRING' and 'LPCAL' and the source OQ208. This step was essential because of the large (roughly 30%) leakage at the GBT at this frequency. 'LPCAL' solves for a single leakage value per subband, whereas the GBT polarization leakage varies across the 128-MHz subband; accordingly, we split each 128-MHz subband into four 32-MHz subbands to allow a coarse frequency dependence to the leakage solutions.

We solved for time-dependent delays using 'FRING' on the primary gain calibrator J1258–2219, followed by self-calibration on this source using 'CALIB', obtaining a single solution per subband per scan. Finally, we improved the phase calibration using self-calibration on the secondary gain calibrator J1312–2350, deriving a single frequency-independent solution per scan.

At each stage, the solutions from the SN table were applied to the CL table using 'CLCAL'. The final CL table was applied to the target using 'SPLIT'. The target was then exported in UVFITS format using 'FITTP' and imaged using 'difmap'[32].

VLA/VLBI interferometric data processing. We processed using VLA cross-correlated data (with the WIDAR correlator) using a custom-developed pipeline, which incorporates manual flagging, and standard interferometric data-calibration techniques in CASA. The imaging was done with the CASA task clean with natural weighting, choosing an image size of 4,096 pixels × 4,096 pixels and a cell size of 0.5 arcsec.

The VLA-only data give the GW170817 flux densities of 56 ± 8 μJy beam^{-1}, 54 ± 8 μJy beam^{-1} and 45 ± 7 μJy beam^{-1} for the three observations of the third epoch at 4.5 GHz. All three observations combined give 55 ± 5 μJy beam^{-1}. For the four observations of the fourth epoch, the flux density values are 55 ± 8 μJy beam^{-1}, 46 ± 8 μJy beam^{-1}, 48 ± 6 μJy beam^{-1} and 46 ± 6 μJy beam^{-1}; all four observations combined give 48 ± 4 μJy beam^{-1}.

Flux comparison between the VLBI and VLA interferometric data. A comparison between the flux densities measured in the VLA-only interferometric data and those measured in the VLBI data (see Extended Data Table 1) implies that, within 1σ uncertainties (typically 10% of the source flux density), no flux is being resolved out in the VLBI data.

Model fits and parameter estimates. Difmap[32] was first used to produce a 'dirty' (un-deconvolved) image from the concatenated data from each epoch and the individual observations within each epoch. In the first two epochs, there was substantial loss of sensitivity owing to technical issues, and the source was not detected. We place 5σ upper limits of 40 μJy beam^{-1} (1.6 GHz, day 38) and 60 μJy beam^{-1} (3.2 GHz, day 52) on the flux densities of GW170817, and do not consider these epochs further.

In the third and fourth epochs, a radio counterpart to GW170817 can clearly be seen in the dirty images for the concatenated datasets, and the source can also be seen (albeit at low signal-to-noise ratio) in the individual observations. Initially, we fit the data in the visibility plane using a single circularly symmetric Gaussian model component. Although probably an over-simplification of the true source structure, this has the advantage of being fast and simple to fit, while providing an accurate estimate of the flux centroid position. After model fitting, we read the resultant clean image into AIPS and used the task JMFIT to fit an elliptical Gaussian in the image plane. Compared to model fitting, this has the advantage of providing well-constrained estimates of the uncertainty of the key parameters of interest[33]. In the third epoch (day 75), the best-fit values of flux density and position are 58 ± 5 μJy beam^{-1}, RA = 13 h 09 min 48.068638(9) s and dec. = −23° 22′ 53.3909(4)″. The uncertainties given here are purely statistical; we consider systematic contributions in the following sections. The best-fit size was a full-width at half-maximum (FWHM) of 0.0 mas; that is, the source was modelled as a point source. At day 230, the best-fit values of flux density and position are 48 ± 6 μJy beam^{-1}, RA = 13 h 09 min 48.068831(11) s and dec. = −23° 22′ 53.3907(4)″, and the best-fit de-convolved size is 0.7 mas, although an unresolved source could not be excluded. The images of the source at days 75 and 230 are shown in Extended Data Fig. 1.

Estimating systematic contributions to flux density and position uncertainties. The absolute calibration of flux densities in VLBI maps can be challenging owing to the fact the sources compact enough to be visible at milliarcsecond resolution typically evolve on a timescale of months to years. In cases where only a priori amplitude calibration can be performed, the accuracy of the flux density scale of a VLBI image is typically assumed to be roughly 20%. In this case, we are able to use the contemporaneous VLA data to establish an absolute flux density scale, using the calibrator sources J1312−2350 and J1258−2219 (under the assumption that these sources do not have substantial structure on scales larger than that resolvable by our VLBI observations). After adjusting the VLBI amplitude scale to produce the closest match to these two sources, the residual differences are typically 10% for each observation, and hence systematic uncertainties on our measured values of flux density for GW170817 are comparable to our statistical uncertainties.

Similarly, for our image centroid positions, we must consider the possibility of systematic position shifts between epochs owing to calibration errors, in addition to the limiting precision attainable on the basis of the image resolution and signal-to-noise ratio. We neglect systematic errors due to the uncertainty in the calibrator reference position, because this would affect both epochs equally. Given the relatively close proximity of our calibrator source J1312−2350 to GW170817 (0.8°), we expect any systematic errors that vary between epochs to be at most a small fraction of the synthesized beam size. Astrometric simulations[34] suggest a typical systematic error for a single observation with the VLBA of 0.07 mas in RA and 0.25 mas in dec. for our observing conditions (dec. = −26°, angular separation of 0.8°). However, these simulations do not include the effect of the ionosphere, which could treble the systematic error at an observing frequency of 4.5 GHz under typical conditions. Countering this, our epochs consist of 3–4 observations spread over about 7 days, and systematic errors (in particular those due to the ionosphere) are likely to be only weakly correlated over this timescale. On the basis of these considerations, we estimated the systematic position uncertainty to be 0.15 mas in RA and 0.5 mas in dec., and added this value in quadrature with the formal position fit errors at each epoch.

To verify this expectation, we repeated the data reduction for the third and fourth epochs after shifting the phase centre of our target field to the position of the NGC 4993 low-luminosity active galactic nucleus. This source is separated by 10.3 arcsec from GW170817, and hence falls outside the field of view of the phased VLA; accordingly, the VLA was flagged before imaging. The positions obtained for the active galactic nucleus have a separation of 0.05 mas in RA and 0.5 mas in dec. (see Extended Data Fig. 2). This is consistent with both their statistical uncertainties and our estimate for the systematic errors derived above. The flux density of the active galactic nucleus is consistent with a constant value (0.25 ± 0.02 mJy and 0.29 ± 0.03 mJy in the third and fourth epochs, respectively, where the 1σ uncertainties are purely statistical).

Comparison between the VLBI data and synthetic images. To compare the models with our VLBI data, we converted the simulated images (example images shown in Fig. 3; for details of the simulations see the next section) into difmap models consisting of point sources at the centre of each non-zero pixel in the simulated image, and performed model fitting in the visibility plane. The rotation, translation and total flux density of the image were taken as free parameters, although we used the approximate positions and flux densities from our earlier fitting of circular Gaussian components to restrict the ranges of parameter values over which we searched. For each model, we recorded the χ^2 obtained at the best-fit values for rotation, translation and total flux density.

Because the signal-to-noise ratio of each individual visibility measurement is very low, determining the increase in χ^2 that indicates a significant discrepancy between models is not straightforward. Previous authors have often relied on visual inspection of images and visibility data to determine model goodness-of-fit[35,36]. Owing to the low signal-to-noise ratio of our target image, we took a different approach. First, we used an image-plane fit to determine the position errors in the image plane using the dataset fitted with a circular Gaussian component, which is a well-understood process[33]. Second, we perturbed the position of the circular Gaussian model component by up to $\pm 3\sigma$ in RA and $\pm 3\sigma$ in dec., and recorded the change in χ^2 at offsets of 1σ, 2σ and 3σ. A consistent increase in χ^2 was seen regardless of the direction of the positional perturbation. Finally, we fitted other models based on the hydrodynamic simulations to the data and recorded the χ^2 in each case. The reference positions for a given model were allowed to vary between the day-75 and day-230 datasets by up to the amount of our estimated systematic position uncertainty of 0.15 mas in RA and 0.5 mas in dec. By comparison to the set of χ^2 values obtained from the perturbed circular Gaussian fits, we estimated the consistency of each hydrodynamic model with the best-fitting circular Gaussian model.

In addition to fitting the actual synthetic images, we first produced an estimate of the maximum source extent, by finding the largest circular and elliptical Gaussian sources that produced a χ^2 that did not deviate by more than 1σ from the best circular Gaussian fits. For the epochs at day 75 and day 230, the largest circular Gaussian source was 1.1 mas and 1.2 mas in diameter, respectively. The best-fitting elliptical Gaussian converged to an unphysical one-dimensional source for each epoch, with an upper limit on the major axis of 12 mas and 9 mas for day 75 and day 230, respectively. In both cases the best-fit position angle was approximately aligned with the major axis of the beam and hence approximately perpendicular to direction of source motion. Tighter limits on the maximum size can be obtained if the axial ratio of the elliptical Gaussian source is constrained to a physical value: for instance, in the case of the day-230 dataset, the largest source permitted with an axial ratio of 4:1 is 3.9 mas $\times$ 0.9 mas. Hence, the source size parallel to the direction of motion is relatively well constrained.

None of the synthetic images produced a χ^2 significantly better than a simple circular Gaussian in either epoch (unsurprising, given that the source was consistent with being unresolved in both cases). Generally, we found that as the positional offset between days 75 and 230 increased, the best-fit source size at day 230 also increased and was often inconsistent with the observed compactness of the source. This disfavoured models at low viewing angles. Conversely, models at large viewing angles were incapable of producing a sufficiently large positional offset.

The best-fitting model (narrow jet viewed at 0.35 rad, model A1 in Figs. 2 and 3) was able to produce the expected positional shift between epochs: with a constant reference translation and rotation, it produced an acceptable fit to both the day-75 epoch (χ^2 increase equivalent to a 0.9σ position offset for the circular Gaussian) and the day-230 epoch (χ^2 increase equivalent to a 1.3σ position offset for the circular Gaussian). Of the other models, only one (model B, the very narrow jet viewed at 0.3 rad) remained consistent within 2σ for both epochs. For all other models, the discrepancy with the best-fitting circular Gaussian exceeded 2σ in one or both epochs. As can be seen in Fig. 2, models A1 and B are also those that best fit the light curve.

Numerical hydrodynamic simulations. To characterize the properties of different models, we carry out relativistic hydrodynamical simulations of various set-ups, followed by a post-processing numerical calculation[28] of their afterglow light curve and observed images at 75 and 230 days. In particular, we run different types of model to see which have the potential to fit the entire dataset of both the light curve and the image characteristics, that is, the flux centroid movement and the image size constraints.

Our set-up includes three components: the jet, a core of cold massive ejecta and a fast ejecta tail. Each component of the ejecta expands homologously and has a density profile of

$$\rho(r,\theta) = \rho_0 r^{-\alpha}\left(\frac{1}{4} + \sin^{\beta}\theta\right)$$

where the normalization ρ_0 is determined by the total ejecta mass, and α and β, which differ between models, dictate the radial and angular structures, respectively. However, our main focus was on scanning the properties of jets, such as luminosities, opening angles, injection and delay times. Although some of the jets successfully break out from the ejecta if their properties allow, others may be choked inside it. We ran about ten different models; here we present four representative models that demonstrate how the different characteristics of the jet affect the observed outcome. The first two models are narrow jets and are found to fit all of the observed characteristics—the gradual rise of the flux, the short plateau at the peak followed by a fast decline and the large flux centroid motion between the two image epochs. In addition, we present a wider successful jet and a choked jet. The full set-up is given in Extended Data Table 2.

A full description of the hydrodynamic simulations is given in our previous work[28]. In brief, for each model we use three different simulations. The first one, which includes the jet propagation inside the core ejecta, is performed in three dimensions to avoid the numerical plug artefact[37]. The second simulation includes the outflow evolution inside the tail ejecta and after breaking out of it until reaching the homologous phase. This simulation is modelled in two dimensions because after breakout the plug artefact is no longer a concern[38], and two- and three-dimensional simulations become similar. Finally, the third simulation begins when the afterglow becomes important and ends after it decays.

For the relativistic hydrodynamical simulation we use the public code PLUTO[39] v4.0 with an Harten–Lax–van Leer Riemann solver and apply an equation of state with an adiabatic index of 4/3. The set-up of models A and B is as follows. The grid set-up of the first three-dimensional Cartesian simulation has three patches on the x and y axes and two patches on the z axis. On x and y the inner patch spans from -2×10^{8} cm to 2×10^{8} cm with 30 uniform cells. The outer patch is from $|2\times10^{8}\,\mathrm{cm}|$ to $|3\times10^{10}\,\mathrm{cm}|$ with 400 cells that are distributed logarithmically. On the z axis the first patch is uniform from 4.5×10^{8} cm to 10^{10} cm with 200 cells, followed by a logarithmic patch of 400 cells until 4×10^{10} cm. We convert the three-dimensional output of the first simulation to an axisymmetric grid[38], which is the initial set-up of the second simulation, for which the set-up is as follows. The first two patches on the r and z axes correspond to the three-dimensional set-up. We add another patch on each axis from 3×10^{10} cm (4×10^{10} cm) on the r (z) axis to 6×10^{11} cm, with 1,200 logarithmic cells.

For the third simulation, which includes two patches on each axis, we use the output of the second simulation. The first patch corresponds to the second simulation grid with 800 uniform cells until $6\times10^{11}\times R$ cm on each axis. The second patch on each axis stretches to $10^{14}\times R$ cm with 6,000 logarithmic cells. Because the simulation is dimensionless, we use R as a scaling length factor[28]; R also determines the density of the interstellar medium (ISM), which is set to be $\rho_{\mathrm{ISM}} = 5\times10^{-12}\,\mathrm{g}\times(R\times\mathrm{cm})^{-3}$ in simulation A and $\rho_{\mathrm{ISM}} = 8\times10^{-12}\,\mathrm{g}\times(R\times\mathrm{cm})^{-3}$ in simulation B. Each viewing-angle fit requires a different R. The best fits for $\theta_{\mathrm{obs}} = 0.25$, 0.35 and 0.45 in simulation A are obtained at $R = 3\times10^{5}$, 1.7×10^{5} and 8.3×10^{4}, respectively; for $\theta_{\mathrm{obs}} = 0.3$ in simulation B it is $R = 5\times10^{5}$.

The set-up of simulations C and D has been described previously[28] (simulation D is identical to the successful-jet scenario, except for the engine time), and the only difference here is that for the outer patch in the third part we use a high resolution of 4,000 cells rather than the 2,500 cells used originally. The scaling of the third part of the simulation is determined by $n = 4\times10^{-2}\,\mathrm{cm}^{-3}$ and $n = 4.5\times10^{-3}\,\mathrm{cm}^{-3}$ in C and D, respectively.

Finally, we verify that each of the three simulations meets the required resolution to reach convergence. We first compare the resolution of the first two simulations, from the jet launch until reaching the homologous phase, with previously published simulations[37] for which convergence tests have been done. The resolution of the three-dimensional simulation that handles the jet propagation inside the ejecta is comparable with that of the inner parts of the previous simulations. The sequential two-dimensional simulation naturally has a higher resolution compared with the outer parts of the three-dimensional grid presented previously[37]. For convergence of the third part in which the outflow interacts with the ISM, we perform another set of simulations with 2/3 of the aforementioned resolution. We find that both the light curves and the images for the relevant viewing angles remain essentially unchanged with the increase in resolution.

Details of the simulation that provides the best fit to the data. Our simulation that provides the best fit to the data is of a jet with a 0.08-rad (4°) opening angle, at the time of light curve peak, that is observed at a viewing angle of $\theta_{\mathrm{obs}} = 0.35$ rad (20°). In this simulation, a relativistic jet is injected into the sub-relativistic merger ejecta. The jet is followed during its propagation through the ejecta, the formation of the cocoon and the breakout of the jet and the cocoon from the dynamical (sub-relativistic) ejecta. The simulation then continues to follow the interaction of the outflow (jet + cocoon) with the ISM. When this interaction starts, the opening angle of the jet is 0.04 rad. The cocoon dominates the observed radio emission during the first approximately 60 days, after which time the jet dominates. The jet expands sideways slowly during its interaction with the ISM, reaching an opening angle of 0.08 rad after about 150 days at the light-curve peak. On day 75, the Lorentz factor of the observed region is $\Gamma \approx 4$, which steadily drops to $\Gamma \approx 3$ by day 230.

Constraining the jet energy and the external density. The γ-ray signal from GW170817 had an isotropic equivalent energy of 5×10^{47} erg. The afterglow suggests that this energy is not representative of the jet energy. This is consistent with models for the γ-ray emission[11,38,40–44]. Therefore, to constrain the jet energy and external density, we use the constraints on the geometry of the outflow together with the observed afterglow light curve to constrain the outflow energy. We use the standard afterglow model, where a narrow ultra-relativistic jet drives a blast wave into the external medium, which radiates in synchrotron emission to produce the radio and X-ray afterglow. Before interacting with the external medium, the jet has an initial Lorentz factor Γ_0. This is also the initial Lorentz factor of the blast wave that it drives, which is constant at first, until the blast wave accumulates enough mass and starts decelerating. The initial opening angle of the jet $\theta_{j,0}$ is also constant until the Lorentz factor drops to about $1/\theta_{j,0}$. At this point, if $\theta_{j,0} < 0.05$ rad the jet starts spreading sideways rapidly until $\theta_{j,0} \approx 0.05$ rad, at which point it starts spreading sideways more slowly[45]. We have direct constraints on Γ and θ_j only near the time of the peak of the light curve. We can therefore put only a lower limit on the initial Lorentz factor, $\Gamma_0 > 4$, and an upper limit on the initial opening angle, $\theta_{j,0} < 0.1$ rad. Moreover, given the fast spreading of the jet if $\theta_{j,0} < 0.1$ rad and $\Gamma < 1/\theta$, at the time that we observe the jet its opening angle is expected to be $\theta_j \approx 0.05$–0.1 rad even if initially $\theta_{j,0} \ll 0.1$ rad and $\Gamma_0 \gg 4$. The Lorentz factor and the time of the peak provide a relation between the density of the ambient medium (assumed to be constant) and the isotropic equivalent energy of the jet[19]: $E_{iso} \approx 10^{52} n/(3 \times 10^{-4} \mathrm{cm}^{-3})$ erg. The flux is extremely sensitive to the Lorentz factor and we can use its value at the peak to constrain the density and the fraction of the internal energy that goes to the magnetic field[19], ε_B: $n/(3 \times 10^{-4} \mathrm{cm}^{-3}) \times (\varepsilon_B/10^{-3})^{0.47} \approx (\Gamma/3.5)^{5.9}$, where we assume that 10% of the internal energy goes to the accelerated electrons ($\varepsilon_e = 0.1$) and that their distribution power-law index is $p = 2.16$. By allowing the least-constrained parameter, ε_B, to vary between 10^{-2} and 10^{-5}, we find that the circum-merger density is 10^{-4}–5×10^{-3} cm^{-3} and that the jet isotropic equivalent energy is $E_{iso} \approx 3 \times 10^{51}$–$10^{53}$ erg. Because the opening angle of the jet at this time is 0.05–0.1 rad and because the jet contains a substantial fraction of the total energy of the relativistic outflow (jet + cocoon), we find that the energy deposited by the merger in relativistic ejecta is 10^{49}–10^{50} erg. The confirmation of a successful jet in GW170817 also implies high isotropy of the magnetic field[46].

Code availability. The hydrodynamic simulations were done using the publicly available code PLUTO. Radio data processing software used were AIPS, DIFMAP and CASA.

Data availability. All relevant (VLBI) data are available from the corresponding authors on request. The VLA data (presented in Fig. 2) are currently being readied for public release.

31. Greisen, E. W. in *Information Handling in Astronomy – Historical Vistas* (ed. Heck, A.) 109–126 (Kluwer Academic, Dordrecht, 2003).
32. Shepherd, M. C. Difmap: an interactive program for synthesis imaging. *ASP Conf. Ser*. **125**, 77–84 (1997).
33. Condon, J. J. Errors in elliptical Gaussian FITS. *Publ. Astron. Soc. Pacif*. **109**, 166–172 (1997).
34. Pradel, N., Charlot, P. & Lestrade, J.-F. Astrometric accuracy of phase-referenced observations with the VLBA and EVN. *Astron. Astrophys*. **452**, 1099–1106 (2006).
35. Tzioumis, A. K. et al. VLBI observations at 2.3 GHz of the compact galaxy 1934-638. *Astron. J*. **98**, 36–43 (1989).
36. Tingay, S. J., Preston, R. A. & Jauncey, D. L. The subparsec-scale structure and evolution of Centaurus A. II. Continued very long baseline array monitoring. *Astron. J*. **122**, 1697–1706 (2001).
37. Gottlieb, O., Nakar, E. & Piran, T. The cocoon emission – an electromagnetic counterpart to gravitational waves from neutron star mergers. *Mon. Not. R. Astron. Soc*. **473**, 576–584 (2018).
38. Gottlieb, O., Nakar, E., Piran, T. & Hotokezaka, K. A cocoon shock breakout as the origin of the γ-ray emission in GW170817. *Mon. Not. R. Astron. Soc*. **479**, 588–600 (2018).
39. Mignone, A. et al. PLUTO: a numerical code for computational astrophysics. *Astrophys. J. Suppl. Ser*. **170**, 228–242 (2007).
40. Lazzati, D. et al. Off-axis prompt X-ray transients from the cocoon of short gamma-ray bursts. *Astrophys. J*. **848**, L6 (2017).
41. Eichler, D. Testing the viewing angle hypothesis for short GRBs with LIGO events. *Astrophys. J*. **851**, L32 (2017).
42. Kathirgamaraju, A., Barniol Duran, R. & Giannios, D. Off-axis short GRBs from structured jets as counterparts to GW events. *Mon. Not. R. Astron. Soc*. **473**, L121–L125 (2018).
43. Bromberg, O., Tchekhovskoy, A., Gottlieb, O., Nakar, E. & Piran, T. The γ-rays that accompanied GW170817 and the observational signature of a magnetic jet breaking out of NS merger ejecta. *Mon. Not. R. Astron. Soc*. **475**, 2971–2977 (2018).
44. Pozanenko, A. S. et al. GRB 170817A associated with GW170817: multi-frequency observations and modeling of prompt gamma-ray emission. *Astrophys. J*. **852**, L30 (2018).
45. Granot, J. & Piran, T. On the lateral expansion of gamma-ray burst jets. *Mon. Not. R. Astron. Soc*. **421**, 570–587 (2012).
46. Corsi, A. et al. An upper-limit on the linear polarization fraction of the GW170817 radio continuum. *Astrophys. J*. **861**, L10 (2018).

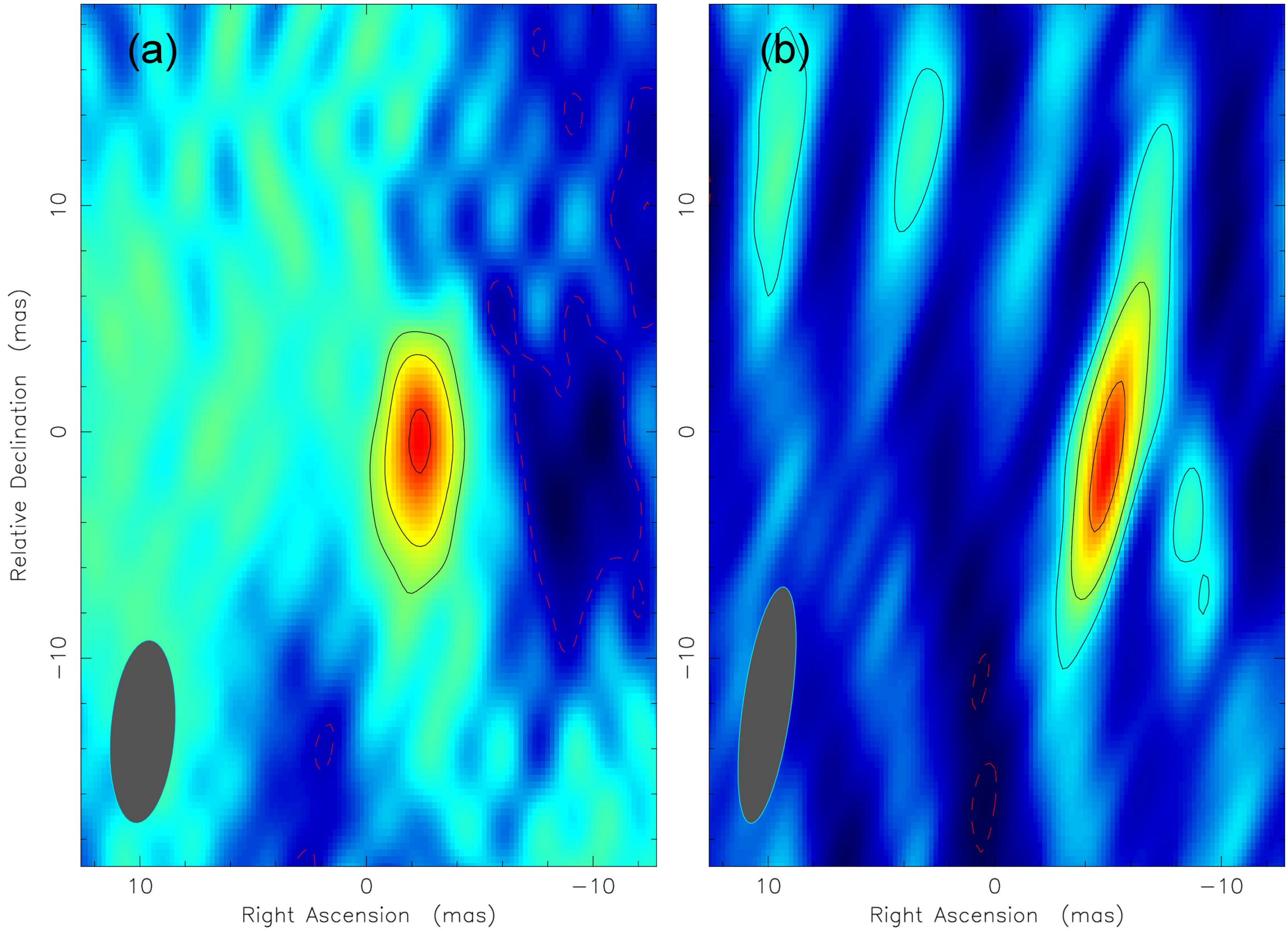

Extended Data Fig. 1 | VLBI images. a, b, The cleaned images (natural weighting; 0.2 mas pixel^{-1}) from the two epochs of VLBI, 75 days (**a**) and 230 days (**b**) post-merger. The centre coordinates for these images are RA = 13 h 09 min 48.069 s, dec. = −23° 22′ 53.39′. The black contours are at 11, 22 and 44 μJy beam^{-1} in both images (red dashed contour is −11 μJy beam^{-1}). The peak flux density of the sources is 58 ± 5 μJy beam^{-1} (**a**) and 48 ± 6 μJy beam^{-1} (**b**) (image root-mean-square noise quoted as the 1σ uncertainty). The ellipse in the lower left corner of each panel shows the synthesized beam: (12.4, 2.2, −7) and (9.1, 3.2, −4) for the two epochs (major axis in mas, minor axis in mas, position angle in degrees).

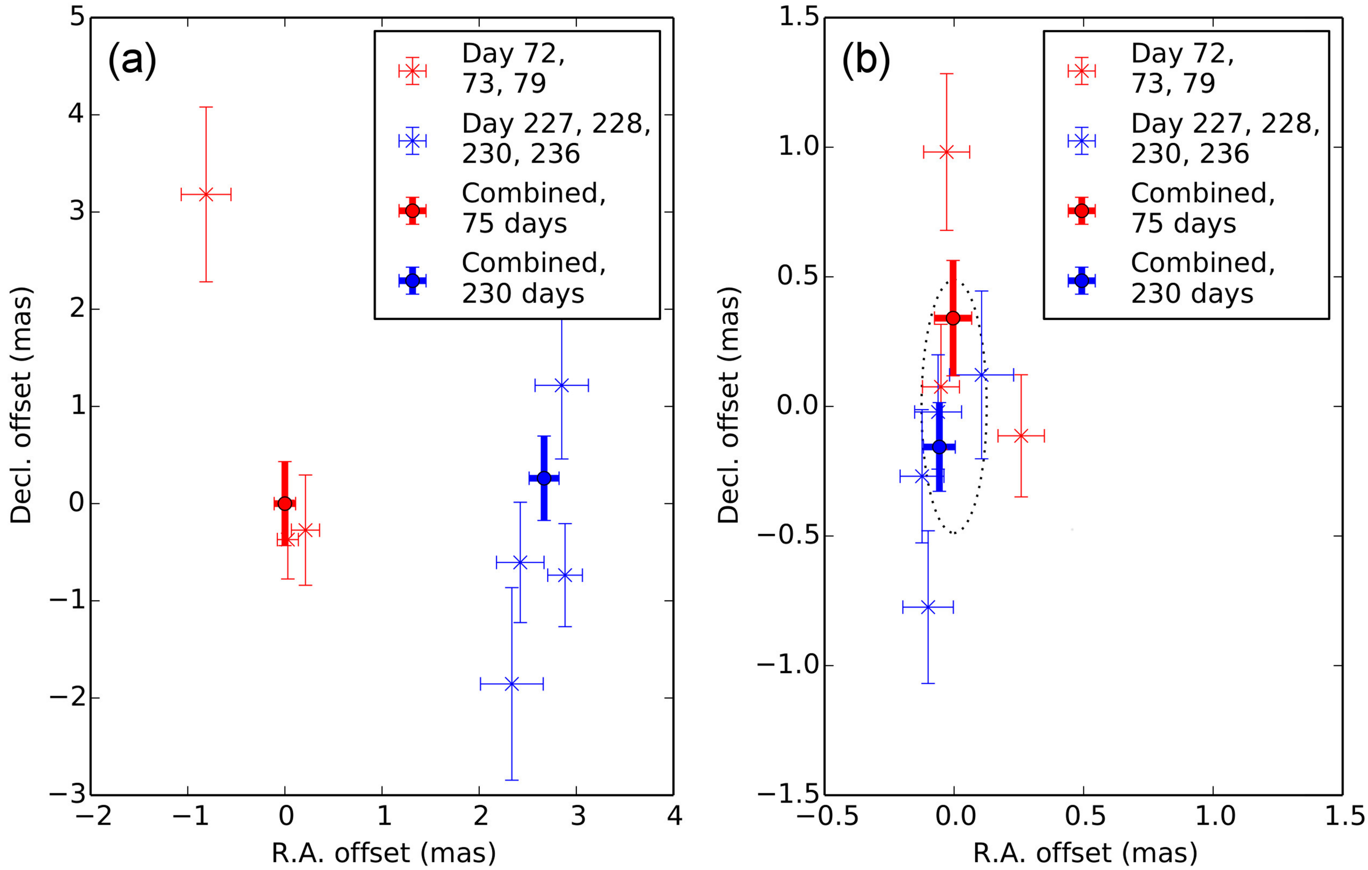

Extended Data Fig. 2 | VLBI astrometric accuracy. a, **b**, The VLBI positions of GW170817 (**a**, relative to the best-fit position at day 75) and the low-luminosity active galactic nucleus in NGC 4993 (**b**, relative to the previously derived position using VLBA-only observations). The individual observations of GW170817 have very low signal-to-noise ratio and hence large errors; the moderately discrepant measurement on day 72 has the lowest signal-to-noise ratio and was affected by observing issues at the GBT. The NGC 4993 positions do not show any significant systematic position shifts between the two epochs, and are consistent with our estimated systematic position uncertainties of 0.15 mas in RA and 0.5 mas in dec. The root-mean-square variation in the position of the nucleus of NGC 4993 over our seven individual observations (0.14 mas in RA and 0.49 mas in dec.) is shown as a dotted ellipse in **b**. All error bars and uncertainties quoted are 1σ.

Extended Data Table 1 | Log of VLBI (HSA) observations

Epoch	Date (UT)	Time (UT)	ν_c (GHz)	BW (MHz)	Δt (days)	F_ν (μJy/beam)	Comments
1	2017 Sep 23	16.5h–22.5h	1.6	256	37	<40	No fringes on the GBT
	2017 Sep 24	16.5h–22.5h			38		
2	2017 Oct 07	15.5h–21.5h	3.2	128	51	<60	VLA mis-configured
	2017 Oct 08	15.5h–18.8h			52		VLA mis-configured
3	2017 Oct 28	14.5h–20.5h	4.5	256	72	58 ± 5	
	2017 Oct 29	14.5h–20.5h			73		
	2017 Nov 04	14.0h–20.0h			79		
4	2018 Apr 01	04.5h–10.5h	4.5	256	227	48 ± 6	VLBA+VLA
	2018 Apr 02	04.5h–10.5h			228		VLBA+VLA
	2018 Apr 04	04.5h–10.5h			230		VLBA+VLA
	2018 Apr 10	04.5h–10.5h			236		VLBA+VLA

ν_c is the centre observing frequency, BW is the effective bandwidth after radio-frequency-interference excision, Δt is the time post-merger and F_ν is the peak flux density of GW170817 (image root-mean-square noise quoted as the 1σ uncertainty; upper limits are 5σ).

Extended Data Table 2 | The initial set-ups of models A–D

Model type	Narrow jets		Wider jet	Choked jet
Model	A	B	C	D
L_j (10^{50} erg)	1.4	0.6	6.7	
θ_{inj}	0.07	0.04	0.18	
t_{inj} (s)	0.2	0.3	0.72	
t_{eng} (s)	0.8	0.6	1.0	0.4
h_j	200	400	80	
M_c ($0.01\,\mathrm{M}_\odot$)	4		5	
M_t ($10^{-3}\,\mathrm{M}_\odot$)	1.6		2.0	
α_c	2		3.5	
α_t	14		10	
β	8		3	
$v_{max,c}/c$	0.2		0.2	
$v_{max,t}/c$	0.6		0.8	

The parameters of the jet are the total luminosity L_j, opening angle upon injection θ_{inj}, injection delay time since the merger t_{inj}, working engine time t_{eng} and specific enthalpy h_j. The ejecta parameters are its mass M, density radial power law $-\alpha$, density angular distribution β and front velocity v_{max}. Each is given for the core with subscript 'c' and tail with subscript 't'.